SAND2016-12818C

Aerodynamic Breakup and Secondary Drop Formation for a Liquid Metal Column in a Shock-Induced Cross-Flow

Yi Chen[1], Edward P. DeMauro[2], Justin L. Wagner[3], Marco Arienti[4]
Daniel R. Guildenbecher[3], Paul A. Farias[5], and Thomas W. Grasser[5]
Sandia National Laboratories, Albuquerque, NM 87185, USA

Patrick D. Sanderson[6]
Iowa State University, Ames, IA 50011, USA

Samuel W. Albert[7]
Purdue University, West Lafayette, IN 47906, USA

Aaron M. Turpin[7] and William Sealy[7]
North Carolina State University, Raleigh, NC 27695, USA

Remington S. Ketchum[6]
University of Arizona, Tucson, AZ 85721, USA

The breakup of liquid metals is of relevance to powder formation, thermal spray coatings, liquid metal cooling systems, investigations of accident scenarios, and model validation. In this work, a column of liquid Galinstan, a room-temperature liquid metal alloy, is studied in a shock-induced cross-flow. Backlit experiments are used to characterize breakup morphology and digital in-line holography is used to quantitatively measure the size and speed of secondary droplets. Two-dimensional simulations are also developed in order to help understand the underlying mechanisms that drive breakup behavior. Results show that although breakup morphologies are similar for water and Galinstan at the same Weber number, the breakup distance, secondary droplet size, and secondary droplet shapes differ. Evidence indicates that secondary droplet formation may be related to the Weber number, density ratio, convective velocity and other effects.

I. Introduction

The aerodynamic breakup of liquids, such as water, have been studied extensively both experimentally and in simulation.[1–3] The forces imparted by the high speed gas tend to distort the liquid surface while the surface tension tends to resist distortions. When the aerodynamic forces exceed the surface tension, the liquid begins to break apart to form secondary droplets. Because droplet atomization is a transient nonlinear hydrodynamic problem, several groups have conducted simulations to determine the breakup mechanisms and critical non-dimensional Weber numbers, Ohnesorge numbers, density ratios, and viscosity ratios.[2,4,5] In simulation,[4] lower density ratios appear to lead to a higher deformation rates while higher density ratios appear to produce more intensive fragmentation. Although a variety of density ratios and Weber number ratios have been simulated, especially for low liquid-to-gas density ratios,[4] there have only

[1]Post-Doctoral Appointee, Engineering Sciences Center, yichen@sandia.gov, Member AIAA.
[2]Post-Doctoral Appointee, Engineering Sciences Center, epdemau@sandia.gov, Member AIAA.
[3]Principal Member of the Technical Staff, Engineering Sciences Center, Senior Member AIAA.
[4]Principal Member of the Technical Staff, Thermal/Fluid Science and Engineering, Livermore, CA 94551.
[5]Laboratory Support Technologist, Engineering Sciences Center.
[6]Graduate Student.
[7]Undergraduate Student.

This work is supported by Sandia National Laboratories and the United States Department of Energy. Sandia National Laboratories is a multi-mission laboratory managed and operated by Sandia Corporation, a wholly owned subsidiary of Lockheed Martin Corporation, for the U.S. Department of Energy's National Nuclear Security Administration under contract DE-AC04-94AL85000.

been a few theoretical studies of liquid metal breakup due to shocks[6–8] and experimental investigations in shock-induced cross flows are limited.[1]

Liquid metals have a variety of unique properties including high densities, high surface tension, and the ability to form oxide skins on the surface.[9] Liquid metal alloys can have complex dynamics because different components in the mixture can melt or crystallize at different temperatures. A eutectic metal is a unique type of alloy that melts at a single temperature lower than the melting points of its constituents. Molten metals also have interesting physics due to the temperature difference between the metal and the surrounding gas. Because of the temperature difference, a vapor film forms around the metal.[7] Combustion mechanisms may also begin to play a part in liquid breakup for high temperatures. Liquid metal breakup characterization is critical for metal powder or droplet production,[9–12] thermal spray deposition,[13–15] liquid metal cooling systems,[16] the study of accident scenarios[6,17] and model validation.[7]

In order to study the effects of increased surface tension and density while minimizing the effects of heat transfer and chemical reactions, we investigate non-toxic metal alloys that are liquid at room temperature. In particular, we consider Galinstan, which is a eutectic liquid metal alloy consisting of gallium, indium and tin. In what follows, the experimental configuration is described and numerical simulations are presented. Next, backlit experiments are used to characterize the breakup morphology while digital in-line holography (DIH) is used to measure properties of the secondary drops. Results show that the Weber number alone does not adequately predict secondary droplet formation phenomena. This study is the first known measurement of liquid metal breakup in a shock-induced cross-flow and presents a unique dataset for model validation.

II. Non-dimensional Scaling

For initially spherical drops, as the Weber number is increased, various droplet breakup morphologies have been observed including vibrational, bag, bag-and-stamen, multimode, sheet-thinning and catastrophic breakup modes.[2,4] The non-dimensional Weber number is defined as,

$$We = \frac{\rho_g u^2 d}{\sigma}, \tag{1}$$

where ρ_g is the gas density, u is the relative velocity between the gas and liquid, d is the characteristic dimension of the liquid, and σ is the interfacial surface tension. The Ohnesorge number is defined as $Oh = \mu_l/\sqrt{\rho_l \sigma d}$, where μ_l is the liquid viscosity and ρ_l is the liquid density. For materials where the Ohnesorge number is small $Oh < 0.1$, such as water and liquid metals, the viscous forces are negligible and the Weber number describes the breakup behavior well.[1,2]

The breakup morphology classifications for liquid column breakup, which is similar to liquid droplet breakup,[2,5] is shown in Fig. 1. For liquid columns in cross-flows, the no-breakup condition is defined by cases where the entire column stays intact while in vibrational breakup, the liquid column breaks up into a few large droplets. Bag breakup is generally defined by the occurrence of a single bag-like shape for every

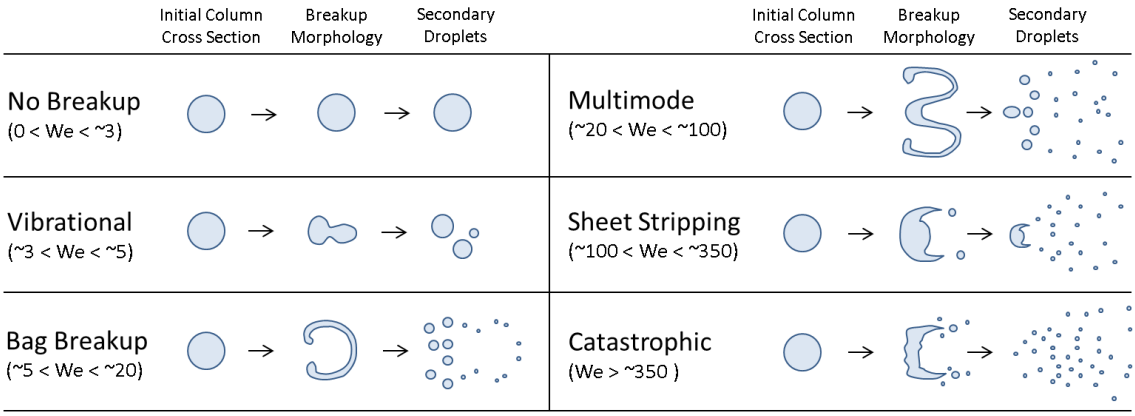

Figure 1. Breakup morphologies and secondary droplet formation classification is shown as a function of the Weber number for liquid column systems where Oh < 0.1. The breakup is viewed from the top of the liquid column.

horizontal slice along the column. If more than a single bag-like shape occurs, the morphology is considered multimode. Lastly, sheet stripping and catastrophic breakup morphologies occur when the edges of the column are accelerated and break up before the center of the column.

When comparing multiple fluids with different densities, a non-dimensional time can be defined as,

$$\tau = \frac{tu}{d}\sqrt{\frac{\rho_g}{\rho_l}} = \frac{tu}{d}\frac{1}{\sqrt{\bar{\rho}}}, \tag{2}$$

where t is the time. The density ratio $\bar{\rho} = \rho_l/\rho_g$ is relevant, especially for low density ratio[4] and high density ratio systems.[9] The non-dimensional time incorporating the density ratio can be derived from analysis of droplet displacement assuming constant acceleration due to drag.[2]

III. Aerodynamic Breakup Simulation

Time-resolved computational fluid dynamics simulations of the liquid column in cross-flow were carried out to assist the interpretation of the experimental results. Here we consider two-dimensional (2D) calculations in order to perform a parametric study with minimum computational expense. In the following, only the evolution of the column cross-section is investigated. Three-dimensional (3D) physics, such as any length-wise perturbations, cannot be captured in these 2D simulations.

To simulate aerodynamic breakup, the compressible Navier-Stokes equations for multi-material flow must be coupled to a sharp-interface method that tracks the gas-metal interface. The piecewise-linear reconstruction of the interface at each time step uses the position of the phase centroids in the computational cell in addition to the liquid volume fraction, following the moment-of-fluid approach.[18] Once the curvature is evaluated, the surface tension is discretized using the ghost fluid method.[19] The Navier-Stokes equations are solved by a semi-implicit, variable density pressure update scheme that asymptotically preserves the incompressible pressure projection in the limit of infinite sound speed.[20] In this way, the stable time step is determined by the flow speed and not by the more restrictive sound speed in the metal. The gas phase is described by the perfect gas equation of state, whereas the liquid metal is described by a generic Tait equation of state for stiff materials. Effects such as oxide films and non-uniformities in liquid properties are ignored.

There are several challenges associated with simulating the break-up of liquid metal by gas crossflow. The first is that the large difference in density and viscosity of the two fluids complicates the discretization of the governing equations at the interface; this situation is exacerbated by the presence of the shear flow induced by the shock. The problem is not only that a large density ratio can result in a more stiff system of equations that is more costly to solve, but that transport inconsistencies between density and velocity cause spurious

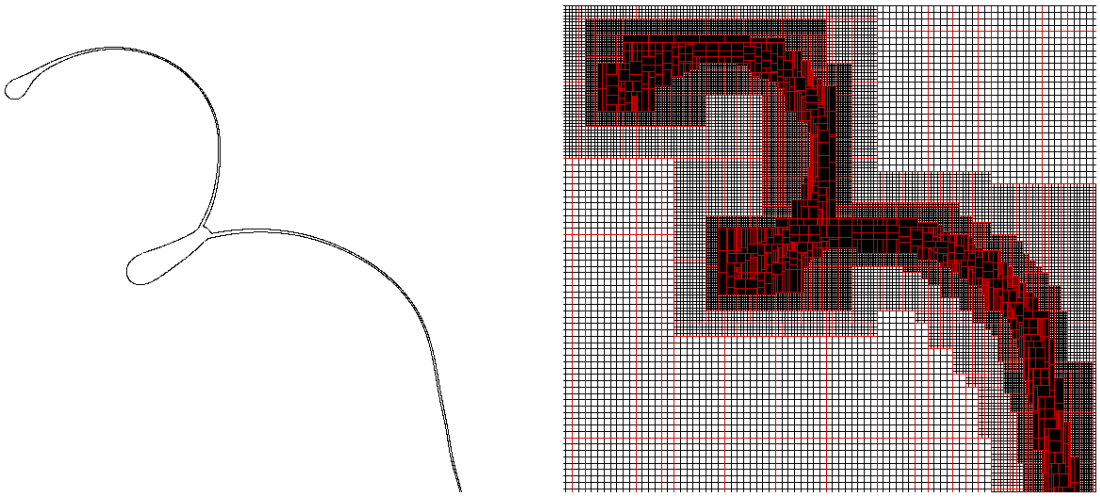

Figure 2. Example of AMR from a solution snapshot is shown. Left: detail of the zero level set curve, representing the gas-metal interface. Right: corresponding arrangement of the Cartesian boxes on four levels of refinement (the box edges are shown in red; the base box does not appear in the field of view).

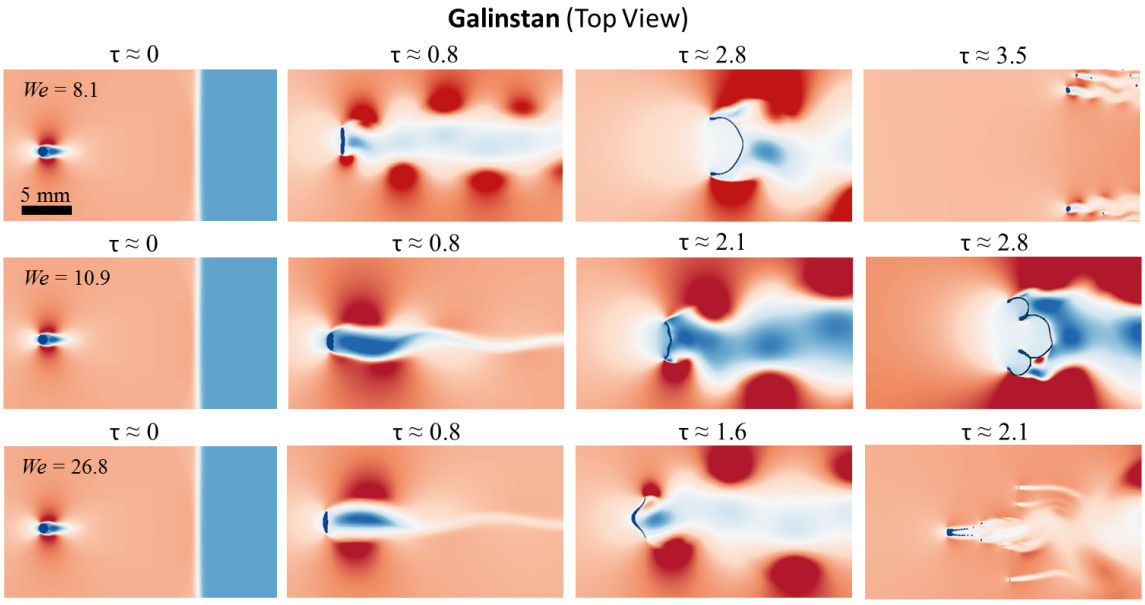

Figure 3. The two-dimensional liquid breakup simulations for Galinstan columns are shown as viewed from the top. The first row shows Galinstan bag breakup for We = 8.1 (Ma = 1.10, u = 54.4 m/s, and ρ_g = 1.14 kg/m^3). The middle row shows multimode breakup for We = 10.9 (Ma = 1.15, u = 80 m/s, and ρ_g = 1.23 kg/m^3). The last row shows sheet stripping breakup for We = 26.8 (Ma = 1.23, u = 119 m/s, and ρ_g = 1.36 kg/m^3). Color contours correspond to the gas velocity in the axial direction.

errors to appear in the solution. Good reviews of past work on different numerical methods to overcome this issue can be found in the literature.[21,22] In the approach adopted here, the directionally split cell integrated semi-Lagrangian algorithm developed in Jemison et al.[20] is coupled with the interface reconstruction to preserve interface sharpness while conserving mass, momentum, and energy of each material. Additional details about the simulation procedure and references to previous work on aerodynamic breakup are available in Arienti et al.,[3] where our numerical approach was first demonstrated for this type of simulation.

A second challenge is that the simulation domain needs to be large enough to include the location where the shock meets the column while also capturing the breakup of the column later downstream. Once breakup occurs, the computational cell size must be small enough to accommodate the size of the secondary particles. This difficulty is mitigated by the adoption of block-structured, adaptive mesh refinement (AMR) procedures that dynamically build higher-density Cartesian meshes where the metal-gas interface occurs. The definitions and the operators necessary to carry out the AMR tasks are provided by the BoxLib library,[23] which is developed to solve partial differential equations on a structured domain by the Center for Computational Sciences and Engineering at Lawrence Berkeley National Laboratory.

In the simulations, the coarsest level (level zero) is always the Cartesian box covering the whole simulation domain. At every new re-meshing operation, a cell-tagging procedure targets the interface; new boxes are combined to cover all the tagged cells within the assigned coverage efficiency. Data on the fine level are either copied from a previous time step or, when a new box is added, they are conservatively interpolated from the underlying coarse level; the refinement ratio between two consecutive levels is two. The new level can in turn be tagged for refinement, and the process is repeated until the input grid resolution is achieved. The gas-metal interface is always embedded in the finest grid level to avoid gross interpolation errors from the calculation of the fluxes of mass, momentum and energy across fine-coarse boundaries.

Calculations were carried out on the 128 SUN X6275 blades (2.93 GHz dual socket/quad core configuration with 12GB RAM per blade) of the Redsky super-computer at Sandia National Laboratories. The initial conditions consist of pure nitrogen driving gas at 300 K with an initial gas density of 1 kg/m^3. The initial cross-section of the liquid column is circular with diameter d =1 mm. The computational domain measures 9.6 cm in the axial direction and 3.2 cm spanwise; the cell count in the two directions is correspondingly 1536 and 512 for level zero. In the course of the simulation, the addition of a level of refinement is triggered (manually) by the cross-section reaching approximately four cells in thickness. By setting a limit of four

refinement levels, this strategy enables us to follow the development of liquid features with a minimum effective grid size of 3.9 μm. Figure 2 shows the junction at a stem of two membranes of Galinstan in multimode breakup. Moreover, the mass of the liquid phase was conserved at least to the fifth significant digit, as confirmed by tracking this value as a function of time.

The simulation results of liquid column breakup for Galinstan are displayed in Fig. 3, where the canonical morphologies of bag, multimode, and sheet stripping can be recognized. By $\tau \approx 0.8$, differences in the shape of the cross-section begin to appear, and by $\tau \approx 1.6$ or later the full shape of the breakup evolves. The bag shapes appear fairly uniform in thickness. As the Weber number increases, the formation of secondary droplets occurs earlier in time. For bag breakup at $We = 8.1$, the secondary droplets appear after $\tau \approx 2.8$. For $We = 26.8$, the predicted generation of secondary droplets, which appear to be semi-spherical, starts near $\tau \approx 1.6$ and evolves steadily past $\tau \approx 2.1$. The morphology classification for both water and Galinstan simulations with comparison to the experiments is reported subsequently.

IV. Experimental Configuration

A. Multiphase Shock Tube

The shock-induced cross-flow experiments are performed in the 76 × 76 mm square cross-section and 5.2 m long Multiphase Shock Tube at Sandia National Laboratories[24,25] as shown in Fig. 4(a). The driver uses pressurized nitrogen, which is released by a fast action valve (Dynamics Systems Research model 725-3.0-6000). The initial conditions of the driven gas are at 300 K and 84.1 kPa. When the shock tube is fired, a planar shock propagates down the driven section, and the convective flow behind the shock wave evolves into an approximate step-change in relative velocity.[26] Eventually, the shock wave rebounds off the solid end wall causing the drop in the convective flow velocity.[27]

B. Fluid Properties and Fluid Delivery

A few liquid metals were considered and Galinstan (RotoMetals LMP-2) was chosen due to its liquid state at room temperature and its relatively low toxicity. Galinstan is a eutectic liquid metal alloy with melting temperatures near -19 °C. The material consists of 68.5% gallium, 21.5% indium and 10% tin and has a reported density of $\rho_l = 6440$ kg/m^3 and a surface tension of $\sigma = 0.718$ N/m at room temperature.[28] The density was also measured in the laboratory and found to be within 3.4% of the reported value. The surface tension was verified using the pendant drop method[29] and found to be within 2.7% of the reported

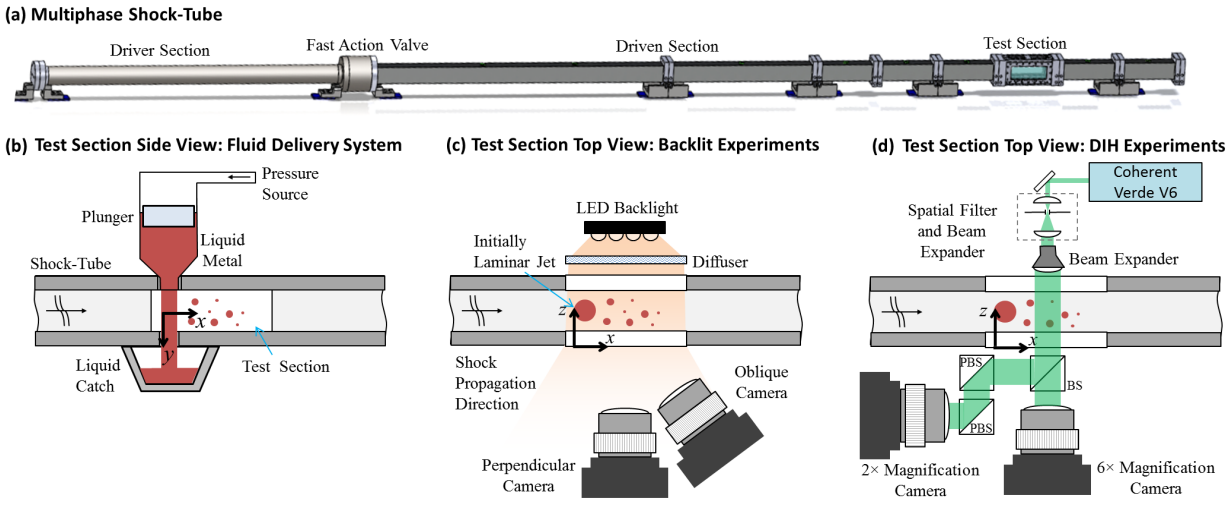

Figure 4. The experimental setup is shown indicating the (a) multiphase shock tube, (b) the side view of the test section showing the delivery system for the liquid metal, (c) the top view of the test section showing the backlit experimental setup, and (d) the digital in-line holography experimental setup. BS - 50/50 nonpolarizing beam splitter, PBS - polarizing beam splitter.

value. The reported viscosity is $\mu_l = 2.4$ mPa $\cdot$ s. Although liquid metals are typically Newtonian,[30] many liquid metals also form oxide skins that may alter the dynamics of the fluid during breakup. Additional precautions were taken to prevent possible chemical reactions between the Galinstan metal and the shock tube components.[31] Acrylic windows were used in the test section and the shock tube sides were covered to prevent gallium from alloying with the aluminum walls. Additionally, where possible, aluminum test section parts were replaced with stainless steel to minimize reactions with the Galinstan.

A laminar jet of liquid must first be established before triggering the shock tube. In prior experiments,[26,32] only de-ionized liquid water is used ($\sigma = 0.073$ N/m and $\rho_l = 1000$ kg/m^3, $\mu_l = 0.89$ mPa $\cdot$ s). When liquid metal is used, a low-volume liquid delivery system is required due to the available quantities of the material. Figure 4(b) shows the simple reservoir and precision fluid dispensing system used for both water and Galinstan experiments. The system is driven using a pressurized air source triggered via a Nordson EFD Performus fluid pump. In order to generate the liquid column, pressurized air (at 1 to 8 psig, depending on the liquid) fills the top of the syringe barrel driving down the plunger thereby dispensing a small amount of liquid through the syringe tip. Before starting an experiment, the velocity of the vertical stream was found to be 2.3 to 2.8 m/s for water and approximately 1.5 to 2.5 m/s for Galinstan, which is significantly less than the convective velocity of the shocks.

C. Backlit Experiments

For the backlit experiments, as shown in Fig. 4(c), two Photron SA-Z cameras (sampling at 100 kHz) were used to obtain high-speed videos. The lighting consisted of an LED backlight and a ground glass diffuser. One camera was placed perpendicular to the flow while the other was placed in an oblique angle. Due to out-of-focus features, the accurate quantification of secondary droplet sizes and velocities from these backlit images is difficult. The overall morphology of the breakup, however, can be evaluated and characterized with the oblique camera.

D. Digital In-Line Holography Experiments

For quantification of secondary droplets, the digital in-line holography setup shown in Fig. 4(d) was used. This system utilizes a 532 nm wavelength Coherent Verde V6 CW laser as the illumination source. The light is spatially filtered using a 100 μm pinhole and the beam is expanded with using a pair of f = 125 mm and f = 400 mm lenses. A second beam expander (Thorlabs GBE03-A) is utilized to further expand the beam and create nearly uniform illumination within the field of view (FOV). Two high-speed cameras at 6$\times$ and 2$\times$ magnification record the stream of secondary droplets. The images on the 2$\times$ and 6$\times$ magnification cameras were acquired at 100 kHz (640 $\times$ 280 pixels) and 20 kHz (1024 $\times$ 1024 pixels) respectively with 0.25 μs exposures.

DIH records the diffraction patterns caused by particles along the line-of-sight. After an experiment, DIH images are numerically refocused to determine the z position of each particle. To do this, a conjugate object wave is first calculated by multiplying the recorded hologram h with the conjugate reference wave E_r^*. Here, the conjugate reference wave is assumed to be constant for the planar reference waves. Next, the reconstructed complex amplitude is numerically propagated to a specific depth z by solving the diffraction equation,

$$E(x, y; z) = [h(x, y)E_r^*(x, y)] \otimes g(x, y; z), \tag{3}$$

where x and y are spatial coordinates, $\otimes$ is the convolution operator and g is the diffraction kernel. The amplitude $A = |E|$ is then used to visualize the refocused image.

A minimum amplitude and maximum Tenengrad method is used to determine where each particle comes into focus. A global optimal threshold is then utilized to determine an initial estimate of size and location. Then, a refinement step is implemented to determine the z locations based on maximum edge sharpness. In order to remove falsely detected and overlapped particles, a second refinement is performed on the z location estimate. Numerical refocusing and particle finding are both computationally intensive processes. To maximize data throughput, processing is done on Sandia National Laboratory's ODIN high capacity MATLAB graphical processing unit (GPU) accelerated computational processing unit (CPU) cluster. Further details and validation of the processing methods are available in Guildenbecher and Gao et al.[33–35]

Automated velocity tracking is accomplished by comparing the particles found on multiple frames. Initial particle matching is determined by creating a cost function that pairs particles to their nearest neighbors in the next frame with a weight function to ensure matched pairs have similar diameters. In order to account for

missing particles, multiple tracks are stitched together based on their projected paths over time. To remove falsely identified tracks and false particles, tracks that do not travel in relatively straight lines in the general direction of the flow are rejected. The algorithm is then iterated in order to combine similar, non-overlapping trajectories. If completely successful, this method tracks each particle once and only once along its entire trajectory through the field of view. With this, it is possible to derive three-dimensional velocity metrics as well as accurately determine the total mass flow without double-counting particles. Details and validation of the methods are available in Guildenbecher et al.[32]

V. Results

A. Backlit Experiments

1. *Qualitative Comparison*

Several experiments with varying liquid column diameters from 0.84 to 1.36 mm were conducted and the resulting breakup regimes were classified. Two figures showing comparisons between Galinstan and water at similar Weber numbers are shown in Fig. 5 for the bag breakup regime and in Fig. 7 for the multimode breakup regime. Since breakup regimes are classified by the initial shape of the column, only small non-dimensional times are considered.

In Fig. 5, the initial stream of Galinstan was subjected to a shock with a speed of Mach 1.12 producing

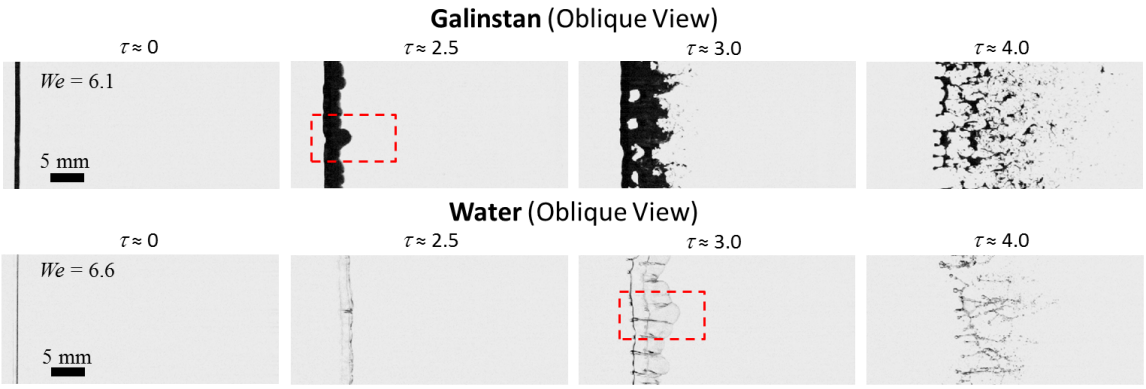

Figure 5. Bag breakup for Galinstan and water with d = 0.84 are shown for We ≈ 6.3 as the liquid column is viewed from the oblique camera. Bag formation and breakup occurs earlier for Galinstan than for water.

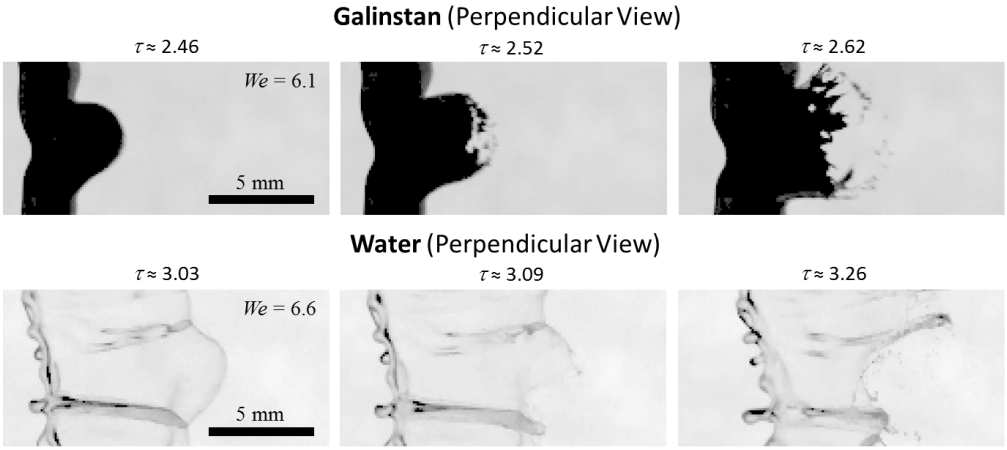

Figure 6. Close-up views of bag breakup for Galinstan and water with d = 0.84 are shown for We ≈ 6.3 as the liquid column is viewed from the perpendicular camera. Both series of images cover a time span of 250 μs and show how a single bag in the column fragments.

a shock-induced convective flow ($u = 66.3$ m/s and $\rho_g = 1.18$ kg/m^3). From the figure, it is clear that the 0.84 mm diameter liquid metal column at $We = 6.1$ appears to be slightly non-uniform at the beginning of the run. This is likely due to the capillary instability, which has a theoretical most unstable wavelength of approximately 4.5 times the jet diameter.[36] Compared to water, the high surface tension of Galinstan likely increases the growth rate of this instability, making it more pronounced in the experiments. Currently, it is unknown if this initial perturbation has any significant effects on the breakup process following the passage of the shock.

At $\tau \approx 2.5$ in Fig. 5 for Galinstan, the first breakup occurs at the thinner parts of the column, forming small bags. Next, the thicker parts of the column also break up into the bag morphology. The overall breakup progression in non-dimensional time is similar to those predicted by the simulation for $We = 8.1$ in Fig. 3. The bags expand and by $\tau \approx 3.0$, they break up or fracture into smaller droplets with irregular shapes. Further downstream, some of these strand-like droplets collide, breakup and recombine. The existence of oxides in the liquid metal or simply non-uniformities in the liquid Galinstan may contribute to these secondary droplet shapes. The oxide layer which forms on Galinstan is elastic and often prevents the fluid from forming spherical droplets.[37,38] Since these effects were not included in the model, these odd secondary droplet shapes were not predicted by the simulation.

The odd shapes of the Galinstan secondary particles may also be partially related to their Oh numbers, which are typically three times lower than that of water. For these test conditions, the Ohnesorge numbers were $Oh = 3.6 \times 10^{-3}$ and $Oh = 1.2 \times 10^{-3}$ for water and Galinstan respectively. Since the Ohnesorge number relates viscous to inertial forces, lower Oh numbers implies less damping. As the secondary droplets separate from the column and oscillate back and forth, lower damping would also prevent these shapes from becoming spherical on short time scales.

These results can be compared with water breakup at a similar Weber number, produced by a shock speed of Mach 1.04 ($u = 23.5$ m/s and $\rho_g = 1.04$ kg/m^3). For $We = 6.6$, the water breaks up into the canonical forward-facing bags and droplet formation does not occur until later in time near $\tau \approx 3.0$. When the bags finally fragment, the final secondary droplets appear to form more spherical shapes.

Close-up images of the bag formation highlighted in the red boxes in Fig. 5 are shown in Fig. 6. Both series of images cover the same 250 μs time span from the maximum extent of the bags to their fragmentation. The Galinstan bags tend to be much smaller than the water bags, which by conservation of mass indicate that the wall thickness of the water bags may be significantly thinner and the deformation ratio significantly higher. This would likely lead to smaller secondary fragments produced by breakup of the water bags compared to breakup of the Galinstan bags.

Similar comparisons can be made with Weber numbers in the multimode regime, as shown in Fig. 7. The conditions for the Galinstan experiment were Ma = 1.24, $u = 127.8$ m/s and $\rho_g = 1.39\ kg/m^3$. The column breakup occurs earlier in non-dimensional time near $\tau \approx 0.9$. Simulations in Fig. 3 predict that this Weber

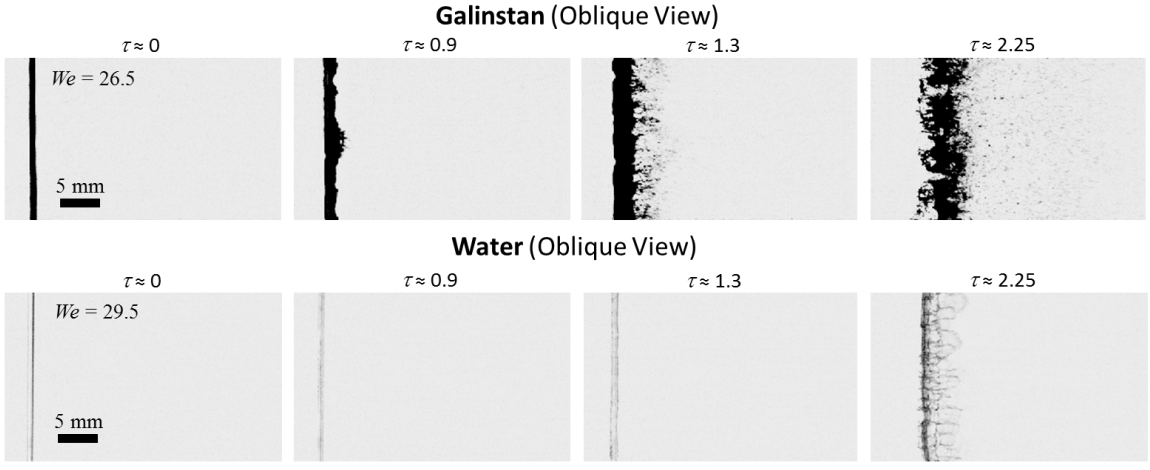

Figure 7. Multimode breakup for Galinstan and water with d = 0.84 are shown for We ≈ 28 as the liquid column is viewed from the oblique camera. Multimode bag formation occurs much earlier for Galinstan than for water.

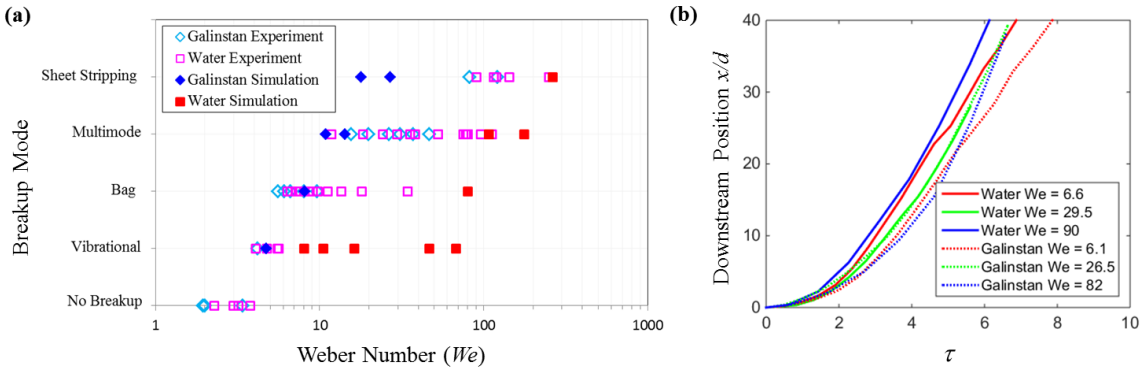

Figure 8. a) Classification of breakup regimes as a function of Weber number for Galinstan and water experiments (d = 0.84 to 1.36 mm) and 2D simulations (d = 1 mm) are shown. Because simulations are 2D, there is no distinction between the no-breakup regime and the vibrational regime as defined in Fig. 1. b) The non-dimensional positions of liquid columns in the x direction are measured as a function of non-dimensional time. The main column downstream position is estimated by selecting the left-most point on the column as it is accelerated by the gas.

number would produce sheet stripping. However, for different points along the column, multiple bags form and break up quickly. Near $\tau \approx 1.3$ at these higher Weber numbers, it is clear that wavelength of the lateral instabilities are significantly less than 4.5 times the jet diameter, indicating that aerodynamic instabilities are also contributing and may be dominating. By $\tau \approx 2.25$, there is a distribution of very small droplets and a separate distribution of larger agglomerates that continue to break up later in time. Again, the Galinstan particles appear to have odd non-spherical shapes.

For water breakup at $We = 29.5$, the flow conditions were Ma = 1.09, $u = 47.9$ m/s and $\rho_g = 1.12\ kg/m^3$. At $\tau \approx 0.9$, the liquid column begins to flatten and perturbations appear on the surface of the column. Multiple bags begin to form at each slice along the column and these bags continue to grow at $\tau \approx 2.25$.

2. Morphology Classification

Several experiments with Galinstan and water were conducted and the Weber number data classified as a function of breakup morphology are shown in Fig. 8(a). The experimental Galinstan and water breakup experiments show similar Weber numbers for each morphology type. Note, due to the inherent uncertainty of determining the breakup morphology from qualitative images as well as potential experimental variability, there is some overlap in the range of Weber numbers over which each morphology type is observed. Similar issues have been observed in previous experiments.[2]

The 2D simulation for Galinstan overlaps well with the experimental measurements up to the sheet stripping regime. Interestingly, when similar simulations were performed for water (closed red squares in Fig. 8(a)), the results tend to over-predict the experimentally observed morphological transition Weber number. Since the simulations are 2D, lengthwise variations and other dynamics cannot be captured. Additional investigation and 3D simulations are required to understand the difference between the experimental data and the simulations.

3. Column Motion

Finally, a few limited quantitative measurements can be extracted from the backlit videos. For example, Fig. 8(b) shows measurements of the left-most point on the column, which faces the gas flow, as a function of non-dimensional time. For the water cases and the Galinstan cases, the results collapse into a single curve. This indicates that the choice of non-dimensional time appropriately captures the convective features of the flow and that existing models for the trajectory[39] may be sufficient for molten metals.

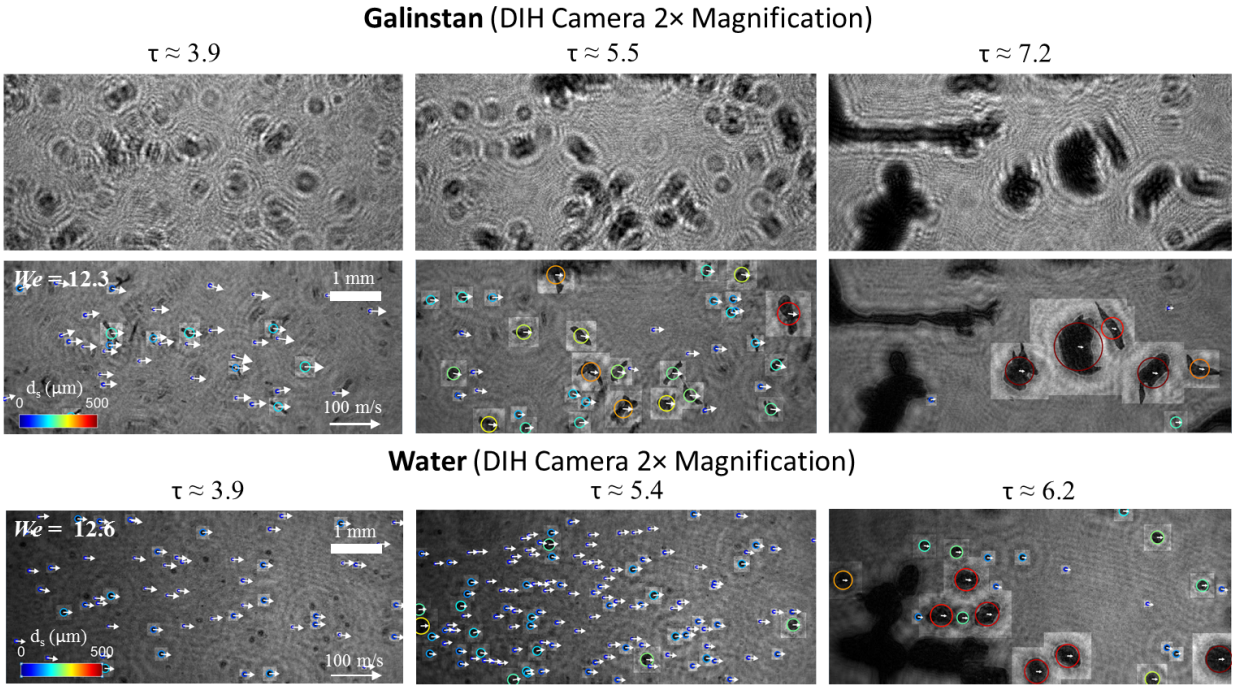

Figure 9. Typical raw holograms (top row) for Galinstan, refocused holograms (middle row) for Galinstan, and refocused holograms for water (bottom row) are shown for a downstream position of approximately 50 mm using the 2× FOV. The refocused holograms also show the tracked particles refocused to their respective z positions and their relative velocities. The colored circles indicate the size of the particle, with smaller particles circled in blue and larger particles circled in red. The experimental conditions are listed in Table 1.

Table 1. DIH Data Experimental Conditions

Material	d (mm)	Driver Pressure (psig)	Ma	u (m/s)	ρ_g (kg/m^3)	We
Galinstan	1.125	15	1.15	80	1.22	12.3
Water	0.94	10	1.05	30	1.09	12.6

B. Digital In-Line Holography

Secondary droplets can be quantitatively measured using DIH techniques. Figure 9 shows several raw and refocused holograms of Galinstan and water flow at Weber numbers between 12.3 and 12.6 at a position that is roughly 50 mm downstream from the initial column. The flow conditions are listed in Table 1. The refocused images include the tracked particles refocused to their respective z planes, the estimated diameter of the particles as a function of their projected pixel area, and their estimated velocity.

Initially, the droplets are fairly small and fast moving. As the flow progresses, the particles become larger and slower. For these DIH experiments, the return shocks are visible in the holography images and arrive at approximately 5.2 to 5.3 ms ($\tau \approx 5.2$ and $\tau \approx 5.4$ for Galinstan and water respectively). These are indicated by the green dotted lines in Fig. 10. Although the gas speeds are slower after the incidence of the return shock, the liquid particles continue to travel forward across the FOV. Near $\tau \approx$ 7.2 for Galinstan and near $\tau \approx$ 6.2 for water, remnants of the columns that have not fully broken up appear.

1. Droplet Diameter and Velocity

The tracked secondary particles can be plotted as a function of non-dimensional time, as shown in Fig. 10, for different positions downstream from the initial column. Secondary droplets first appear around $\tau \approx 2$. At the cameras positioned 20 to 25 mm downstream from the flow, the particle sizes grow rapidly and the largest particles that can be tracked pass by the camera near $\tau \approx 5$, while at roughly 50 mm downstream

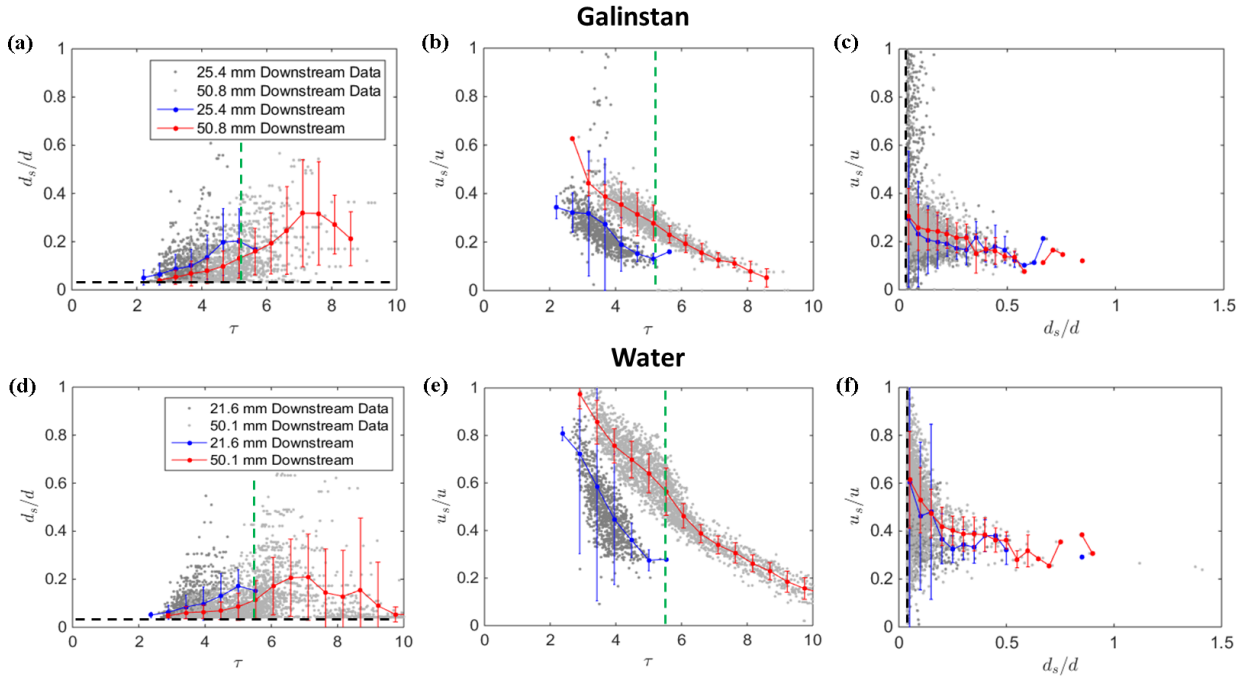

Figure 10. Raw secondary droplet statistics are shown for Galinstan a) non-dimensional diameter d_s/d and b) non-dimensional x direction velocity u_s/u as a function of non-dimensional time. The secondary droplet velocities and diameters are defined as u_s and d_s respectively. c) The non-dimensional diameter as a function of velocity is also plotted. Similarly, the statistics for water d) non-dimensional diameter, e) non-dimensional x velocity, and f) diameter versus velocity are illustrated. Two to three experiments were conducted for each position for each fluid. The flow conditions are listed in Table 1. The black dotted lines indicate the size of the smallest particles that can be measured using the 2× FOV camera. The green dotted lines indicate the approximate incidence time of the return shock at both downstream positions.

the last large particles are observed at around $\tau = 7$ to 10. Note, these times are in good agreement with the non-dimensional time for passage of the intact column shown in Fig. 8(b).

The results in Fig. 10 quantify the phenomena observed in the previous discussion. At early times, secondary fragments are a few tens of micrometers in diameter and are traveling at speeds approaching the gas-flow velocity. These initial drops are almost certainly the result of breakup of the bag structures. At later times, the mean droplet sizes are much larger and are traveling much slower. The late-time fragments almost certainty originate from breakup of the rim like structures and intact core that remain after bag breakup.

The particle diameters can be plotted against their velocities to produce Figs. 10(c) and (f). Although there is a lot of scatter, there is a clear trend in the relationship between the particle size and particle velocity in the x direction. Unlike the water particles which are traveling at faster relative velocities near their convective flow velocities ($u_s/u \approx 0.3$ to 0.6 on average), the Galinstan particles are only traveling at $u_s/u \approx 0.15$ to 0.3 on average.

2. Secondary Droplet Size Distribution

Further details on the breakup dynamics can be obtained by comparing the detailed particle size distributions from the Galinstan and water experiments. To maximize the dynamic range of particle sizes that can be measured, data from both the 2× and 6× fields of view are utilized. With its higher magnification the 6× FOV allows for quantification of smaller diameters. Here it is assumed that the smallest diameter that can be reasonably measured from refocused hologram images is four times the magnified pixel size, leading to a smallest resolvable particle diameter of 13.4 μm. However, due to the high-magnification and relatively slow recording rate, individual particles tend to cross the 6× FOV within a few frames. Therefore, multi-frame particle tracking is performed using the 2× FOV data. As shown by the size-velocity correlations in Figs. 10(c) and (f), the largest diameter fragments tend to travel slowest and will reside in the FOV longer than the smallest diameter fragments. Consequently, larger fragments would be over-counted, resulting in

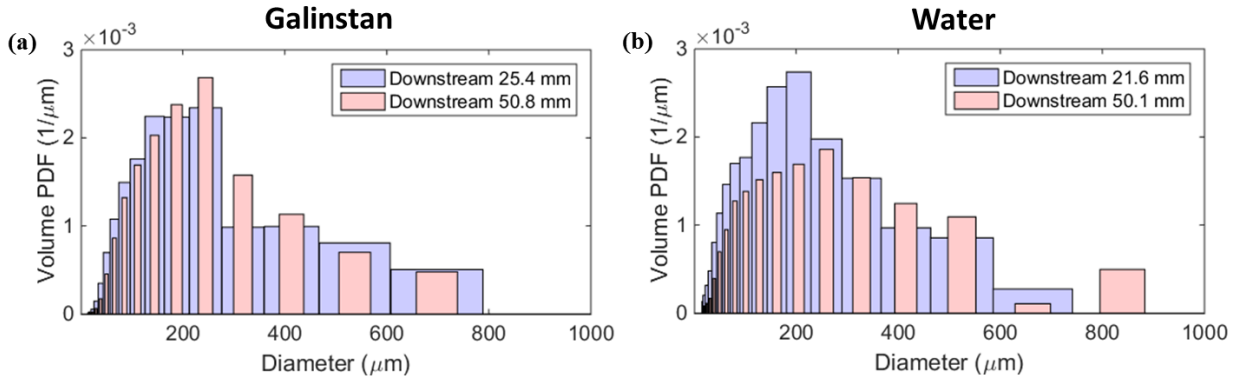

Figure 11. The corrected volume PDFs for Galinstan and water from the 6× FOV data are illustrated at different positions downstream from the initial column for the flow conditions listed in Table 1.

Table 2. Secondary Droplet Mean Diameters

Material	Downstream Position (mm)	Mass Tracked as Secondary Particles* (%)	$D_{10}^{\dagger}$ (μm)	$D_{30}^{\dagger}$ (μm)	$D_{32}^{\dagger}$ (μm)	MMD† (μm)
Galinstan	25.4	22%	83.4	144.2	252.4	315.8
Galinstan	50.8	41%	103.4	167.7	272.9	337.5
Water	21.6	30%	57.7	117.6	242.5	363.3
Water	50.1	76%	71.4	150.8	331.2	503.9

* Corrected values using 2× FOV camera data

† Corrected values using 6× FOV camera data

a size-velocity bias. To correct this, measured fragment diameters from the 6× FOV are weighted by the average residence time for each diameter size class as defined by the 2× FOV (inverse of the average size-velocity correlation shown in Figs. 10(c) and (f)). In this manner, the largest possible fragment size dynamic range is obtained from the 6× FOV, with size-velocity biases removed using velocity measurements from the 2× FOV.

The resulting corrected volume probability distribution functions (PDF) are compared in Fig. 11. Galinstan at 25.4 mm downstream appears to be bi-modal with a group of larger particles centered near 400 μm and a group of smaller particles centered near 200 μm. As noted earlier, the peak at smaller diameters is likely due to fragments generated from breakup of the bag. For water, at the upstream position (21.6 mm) most of the secondary fragments are a few hundred micrometers or less, while slightly larger diameters are observed further downstream (50.1 mm). The evolution of this bi-modal distribution at a further downstream position in the case of water versus Galinstan is quantitative evidence that the breakup process takes longer in the case of water.

The PDFs can also be viewed as quantitative compiled statistics as listed in Table 2. The percentage of mass tracked as secondary particles is measured by summing the mass of the tracked particles and comparing this with the initial mass of a column of height equal to the y-extent of the FOV. Further downstream, more breakup occurs and more mass can be tracked as secondary particles. Finally, for a total of N measured drops, D_{pq} are the characteristic mean diameters defined as,

$$D_{pq} = \left(\frac{\sum d_i^p}{\sum d_i^q} \right)^{\frac{1}{p-q}} . \tag{4}$$

The number population mean is defined as D_{10}, the surface area weighted mean (or Sauter mean) is defined as D_{32} and the volume mean diameter is defined as D_{30}. The mass mean diameter (MMD) is defined as the diameter where half of the total measured volume is composed of drops of a larger diameter. Since D_{32} and MMD more heavily weight larger droplets, these metrics are better indicators of the distribution of bigger droplets in the flow.

Table 2 shows that D_{10} tends to be smaller for water compared to Galinstan, while D_{32} and MMD at the ~ 50 mm position tend to be larger. This may be quantified evidence that breakup of the bag structures tends to produce smaller fragments in typical liquids like water when compared to Galinstan. In addition, the breakup of the rim and other intact core structures tends to produce larger fragments in water than in Galinstan. Of course, more work is needed to investigate these phenomena and in particular quantify experimental uncertainty.

VI. Conclusion

In the literature, there have been few experimental investigations of liquid metal breakup. In this paper, we investigate the aerodynamic breakup of columns of liquid metal Galinstan in a shock-induced cross flow and compare the results with the breakup of water columns. The initial breakup morphologies of Galinstan are qualitatively similar to those of water for $0 < We < 250$ but there are several key differences. First, the incidence of breakup occurs earlier in non-dimensional time for Galinstan and the breakup appears to be more violent. This is consistent with what has been suggested by other simulations in the literature.[4] Instead of forming large, thin bags that break up into spherical droplets like water, Galinstan bags are smaller and appear to fracture, forming non-spherical strand-like secondary droplets.

The sizes of secondary droplets were also characterized using digital in-line holography measurements at different positions downstream of the initial liquid column. Results show that breakup of water tends to produce overall larger mean fragment diameters, particularly with respect to volumetric means that are of most relevance to many combustion and dispersal applications. However, interestingly water also appears more able to sustain stretching and thinning of the bag resulting in smaller fragments from the bag for water compared to Galinstan. Taken together, these observations indicate that scaling relations for the fragment sizes may need to be updated to account for the detailed effects of high surface tension, high density and other attributes of liquid metals.

Two-dimensional simulations were conducted in order to better understand the physical mechanisms that occur during aerodynamic breakup. The simulations provide a good estimate of the initial Galinstan breakup morphology as a function of Weber number as well as predict the non-dimensional time at which the breakup occurs. Although many of the features are successfully captured by the 2D simulations, some differences in the prediction of the incidence of breakup still exist. Bag breakup via fracture and non-spherical droplets may be due to oxides or non-uniformities inside the Galinstan. Incorporating these effects into a 3D model can potentially improve the match between experiments and simulations.

This work has shown that the breakup morphology of liquid metal in a cross-flow is related to the Weber number analogous to what has been previously observed for typical liquids like water. In contrast, the rate of breakup and the size of secondary fragments may display a more complex relationship with other factors, such as density ratio, which have not yet been fully elucidated. Future work in this area includes investigating more flow conditions for Galinstan at higher Weber numbers. Studying the breakup of other liquid metals or other high-density liquids may also help tease apart some of the effects which are due to the eutectic nature of Galinstan from the effects that are driven by density and surface tension. Finally, computationally intensive 3D simulations may be required to better capture the three-dimensional nature of breakup and droplet formation.

VII. Acknowledgments

This project was supported by the Laboratory Directed Research and Development program at Sandia National Laboratories.

References

[1]Hsiang, L.-P. and Faeth, G. M., "Drop Deformation and Breakup Due to Shock Wave and Steady Disturbances," *32nd AIAA Aerospace Sciences Meeting, AIAA SciTech*, 1994, AIAA-94-0560.

[2]Guildenbecher, D. R., López-Rivera, C., and Sojka, P. E., "Secondary Atomization," *Exp. Fluids*, Vol. 46, No. 3, 2009, pp. 371–402.

[3]Arienti, M., Doisneau, F., and Oefelein, J., "Computation of the Break-Up of a Molten Metal Drop under Sudden Acceleration," *ILASS Americas 28th Annual Conference on Liquid Atomization and Spray Systems*, 2016.

[4]Yang, W., Jia, M., Sun, K., and Wang, T., "Influence of Density Ratio on the Secondary Atomization of Liquid Droplets

under Highly Unstable Conditions," *Fuel*, Vol. 174, 2016, pp. 25–35.

[5]Joseph, D. D., Belanger, J., and Beavers, G. S., "Breakup of a Liquid Drop Suddenly Exposed to a High-Speed Airstream," *Int. J. Multiphase Flow*, Vol. 25, 1999, pp. 1263–1303.

[6]Mingjun, Z., Yuan, Z., Meng, L., Minghao, Y., and Yanhua, Y., "Numerical Simulation of Molten Droplet Deformation and Disintegration under Sudden Accelerations," *Ann. Nucl. Eng.*, Vol. 65, 2014, pp. 199–206.

[7]Lin, M., Zhong, M., Li, Y., Yuan, M., and Yang, Y., "Numerical Analysis on Molten Droplet Hydrodynamic Deformation and Surface Waves under High Pressure Pulse," *Ann. Nucl. Energy*, Vol. 77, 2015, pp. 133–141.

[8]Ling, Y., Haselbacher, A., Balachandar, S., Najjar, F. M., and Stewart, D. S., "Shock Interaction with a Deformable Particle: Direct Numerical Simulation and Point-Particle Modeling," *J. Appl. Phys.*, Vol. 113, 2013, 013504.

[9]Yim, P., *The Role of Surface Oxidation in the Break-Up of Laminar Liquid Metal Jets*, Ph.D. thesis, Massachusetts Institute of Technology, 1996.

[10]Mates, S. P., Ridder, S. D., Biancaniello, F. S., and Zahrah, T., "Vacuum-Assisted Gas Atomization of Liquid Metal," *Atomization Sprays*, Vol. 22, No. 7, 2012, pp. 581–601.

[11]Markus, S., Fritsching, U., and Bauckhage, K., "Jet Break Up of Liquid Metal in Twin Fluid Atomisation," *Mater. Sci. Eng.*, Vol. A326, 2002, pp. 122–133.

[12]Luo, J., Qi, L.-H., Zhou, J.-M., Hou, X.-H., and Li, H.-J., "Modeling and Characterization of Metal Droplets Generation by Using a Pneumatic Drop-on-Demand Generator," *J. Mater. Processing Technol.*, Vol. 212, No. 3, 2012, pp. 718–726.

[13]Chen, Y., Liang, X., Wei, S., Chen, X., and Xu, B., "Numerical Simulation of the Twin-Wire Arc Spraying Process: Modeling the High Velocity Gas Flow Field Distribution and Droplets Transport," *J. Therm. Spray Technol.*, Vol. 21, No. 2, 2012, pp. 263–274.

[14]Hussary, N. A. and Heberlein, J. V. R., "Atomization and Particle-Jet Interactions in the Wire-Arc Spraying Process," *J. Therm. Spray Technol.*, Vol. 10, No. 4, 2001, pp. 604–610.

[15]Newbery, A. P. and Grant, P. S., "Large Arc Voltage Fluctuations and Droplet Formation in Electric Arc Wire Spraying," *Powder Metall.*, Vol. 46, No. 3, 2013, pp. 229–235.

[16]Kondo, S., Konishi, K., Isozaki, M., Imahori, S., Furutani, A., and Brear, D. J., "Experimental Study on Simulated Molten Jet-Coolant Interactions," *Nucl. Eng. Des.*, Vol. 155, No. 1-2, 1995, pp. 73–84.

[17]Luna, R. E., Church, H. W., Elrick, R. M., Parker, D. R., Nelson, L. S., and Raabe, O. G., "Combustion and Smoke Formation Following Exposure of Actinide Metals to Explosions," *Proceedings of the Fall Meeting of the Western States Section of the Combustion Institute*, 1976.

[18]Jemison, M., Lock, E., Sussman, M., Shashkov, M., Arienti, M., Ohta, M., and Wang, Y., "A Coupled Level Set-Moment of Fluid Method for Incompressible Two-Phase Flows," *J. Scientific Computing*, Vol. 54, No. 2, 2013, pp. 454–491.

[19]Kang, M., Fedkiw, R. P., and Liu, X.-D., "A Boundary Condition Capturing Method for Multiphase Incompressible Flow," *Journal of Scientific Computing*, Vol. 15, No. 3, 2000, pp. 323–360.

[20]Jemison, M., Sussman, M., and Arienti, M., "Compressible, Multiphase Semi-implicit Method with Moment of Fluid Interface Representation," *J. Computational Phys.*, Vol. 279, 2014, pp. 182–217.

[21]Desjardins, O. and Moureau, V., "Methods for Multiphase Flows with High Density Ratio," *Center for Turbulent Research, Summer Program*, 2010, pp. 313–322.

[22]Raessi, M. and Pitsch, H., "Consistent Mass and Momentum Transport for Simulating Incompressible Interfacial Flows with Large Density Ratios Using the Level Set Method," *Comput. Fluids*, Vol. 63, 2012, pp. 70–81.

[23]BoxLib, `https://ccse.lbl.gov/BoxLib/`.

[24]DeMauro, E. P., Wagner, J. L., Beresh, S. J., and Farias, P. A., "Measurements of Gas-Phase Velocity During Shock-Particle Interactions Using Pulse-Burst PIV," *54th AIAA Aerospace Sciences Meeting, AIAA SciTech*, 2016, AIAA-2016-0793.

[25]Wagner, J. L., Beresh, S. J., DeMauro, E. P., Casper, K. M., Guildenbecher, D. R., Pruett, B. O., and Farias, P. A., "Pulse-Burst PIV Measurements of Transient Phenomena in a Shock Tube," *54th AIAA Aerospace Sciences Meeting, AIAA SciTech*, 2016, AIAA-2016-0791.

[26]Guildenbecher, D. R., Wagner, J. L., Olles, J. D., Chen, Y., DeMauro, E. P., Farias, P. A., Grasser, T. W., and Sojka, P. E., "kHz Rate Digital In-Line Holography Applied to Quantify Secondary Droplets from the Aerodynamic Breakup of a Liquid Column in a Shock-Tube," *54th AIAA Aerospace Sciences Meeting, AIAA SciTech*, 2016, AIAA-2016-1044.

[27]Wagner, J. L., Beresh, S. J., DeMauro, E. P., Casper, K. M., Pruett, B. O., and Farias, P. A., "Time-Resolved PIV in a Shock Tube Using a Pulse-Burst Laser," *11th International Symposium on Particle Image Velocimetry*, 2015.

[28]Karcher, C., Kocourek, V., and Schulze, D., "Experimental Investigations of Electromagnetic Instabilities of Free Surfaces in a Liquid Metal Drop," *International Scientific Colloquium: Modelling for Electromagnetic Processing*, 2003, pp. 105–110.

[29]Liu, T., Sen, P., and Kim, C.-J., "Characterization of Liquid-Metal Galinstan® for Droplet Applications," *IEEE 23rd International Conference on Micro Electro Mechanical Systems (MEMS)*, 2010, pp. 560–563.

[30]Ritwik, *Measuring the Viscous Flow Behavior of Molten Metals under Shear*, Ph.D. thesis, Brunel University, 2012.

[31]Morley, N. B., Burris, J., Cadwallander, L. C., and Nornberg, M. D., "GaInSn Usage in the Research Laboratory," *Rev. Sci. Instrum.*, Vol. 79, 2008, 056107.

[32]Guildenbecher, D. R., Cooper, M. A., and Sojka, P. E., "High-speed (20 kHz) Digital In-line Holography for Transient Particle Tracking and Sizing in Multiphase Flows," *Appl. Opt.*, Vol. 55, No. 11, 2016, pp. 2892–2903.

[33]Guildenbecher, D. R., Gao, J., Reu, P. L., and Chen, J., "Digital Holography Simulations and Experiments to Quantify the Accuracy of 3D Particle Location and 2D Sizing Using a Proposed Hybrid Method," *Appl. Opt.*, Vol. 52, No. 16, 2013, pp. 3790–3801.

[34]Gao, J., Guildenbecher, D. R., Engvall, L., Reu, P. L., and Chen, J., "Refinement of Particle Detection by the Hybrid Method in Digital In-Line Holography," *Appl. Opt.*, Vol. 53, No. 27, 2014, pp. G130–G138.

[35]Gao, J., Guildenbecher, D. R., Reu, P. L., and Chen, J., "Uncertainty Characterization of Particle Depth Measurement Using Digital In-Line Holography and the Hybrid Method," *Opt. Express*, Vol. 21, No. 22, 2013, pp. 26432–26449.

[36]Rayleigh, L., "On the Instability of Jets," *Proc. Lond. Math. Soc.*, Vol. s1-10, No. 1, 1878, pp. 4–13.

[37]Kim, D., Thissen, P., Viner, G., Lee, D.-W., Choi, W., Chabal, Y. J., and Lee, J. B., "Recovery of Nonwetting Characteristics by Surface Modification of Gallium-Based Liquid Metal Droplets Using Hydrochloric Acid Vapor," *Appl. Mater. Interfaces*, Vol. 5, No. 1, 2013, pp. 179–185.

[38]Dickey, M. D., Chiechi, R. C., Larsen, R. J., Weiss, E. A., Weitz, D. A., and Whitesides, G. M., "Eutectic Gallium-Indium (EGaIn): A Liquid Metal Alloy for the Formation of Stable Structures in Microchannels at Room Temperature," *Adv. Funct. Mater.*, Vol. 18, No. 7, 2008, pp. 1097–1104.

[39]O'Rourke, P. J. and Amsden, A. A., "The TAB Method for Numerical Calculation of Spray Droplet Breakup," *Proc. International Fuels and Lubricants Meeting and Exposition*, SAE Technical Paper 872089, 1987.